



ELSEVIER

Available online at [www.sciencedirect.com](http://www.sciencedirect.com)

Journal of Computational Physics xxx (2006) xxx–xxx

JOURNAL OF  
COMPUTATIONAL  
PHYSICS[www.elsevier.com/locate/jcp](http://www.elsevier.com/locate/jcp)

# An efficient and robust implicit operator for upwind point Gauss–Seidel method

Joo Sung Kim, Oh Joon Kwon \*

*Department of Aerospace Engineering, Korea Advanced Institute of Science and Technology (KAIST), 373-1 Guseong-dong, Yuseong-gu, Daejeon 305-701, Republic of Korea*

Received 8 March 2006; received in revised form 26 September 2006; accepted 7 November 2006

## Abstract

An efficient and robust implicit operator for the point Gauss–Seidel method is presented for solving the compressible Euler equations. The new implicit operator was derived by adding a scalar form of artificial dissipation to the upwind implicit side. The amount of artificial dissipation was locally adjusted using a weighting factor based on the solution gradient. For validation, the performance of the new implicit operator was compared in detail with that of several existing implicit operators which have been widely used for solving the flow equations. Numerical experiments showed that the stability and convergence characteristics of the new implicit operator are significantly better than those of other existing implicit operators for calculating flows ranging from subsonic to hypersonic speeds.

© 2006 Published by Elsevier Inc.

**Keywords:** Implicit operator; Artificial dissipation model; Upwind point Gauss–Seidel; Euler equations; Stability and convergence

## 1. Introduction

Most of the implicit methods in computational fluid dynamics are derived by applying the local time linearization to the nonlinear flux terms [1], which can be evaluated using either central-difference schemes or upwind schemes. For central-difference schemes, it is necessary to add artificial dissipation to the explicit operator to suppress the odd–even decoupling and to control the numerical instability associated with the nonlinear discontinuities such as the shock wave. The artificial dissipation models are often described as a blending of second-difference and fourth-difference dissipation terms [2]. An artificial dissipation term is also added to the implicit operator to extend the stability limit imposed by the explicit artificial dissipation. The addition of the implicit artificial dissipation has a significant influence on the stability and convergence characteristics of central-difference implicit methods, even though it does not affect the spatial accuracy of the resultant steady-state solutions. The proper amount of implicit artificial dissipation to be added is closely related to that of the explicit artificial dissipation [3–5].

\* Corresponding author. Tel.: +82 42 869 3720; fax: +82 42 869 3710.  
E-mail address: [ojkwon@kaist.ac.kr](mailto:ojkwon@kaist.ac.kr) (O.J. Kwon).

32 Upwind schemes are dissipative in nature due to their differencing stencil, and thus additional dissipation is  
 33 usually not needed. To obtain steady-state solutions, the consistency of adopting the same numerical splitting  
 34 scheme for both implicit and explicit operators is not required, because the spatial accuracy of the solution is  
 35 dictated solely by the explicit operator. In principle the numerical splitting scheme of the implicit operator  
 36 needs to be selected such that the implicit method exhibits good stability and convergence characteristics  
 37 [6,7]. Similar to the central-difference implicit methods, the performance of upwind implicit methods is also  
 38 expected to be highly dependent on the dissipative property of the numerical splitting scheme adopted in  
 39 the implicit operator, even though explicit control of the amount of the inherent numerical dissipation for  
 40 upwind schemes is a difficult task.

41 Currently, several approximate inversion methods are available, including the alternating-direction implicit  
 42 method [8], the point and line Gauss–Seidel (GS) methods [9], and the Krylov subspace method [10]. Among  
 43 them, the point GS method has been widely used for unstructured mesh topologies [11–13], because it is alge-  
 44 braically simple and does not require any spatial coordinate direction splitting. Previous research works [14–  
 45 17] showed that the performance of the point GS method is very sensitive to the dissipative property of the  
 46 numerical splitting scheme of the implicit operator. When the splitting scheme of the implicit operator is more  
 47 dissipative than that of the explicit operator, the point GS method leads to good stability characteristics, but  
 48 typically yields slow convergence rates, as demonstrated by the lower–upper symmetric Gauss–Seidel (LU-  
 49 SGS) method [15,16]. In this method, the implicit operator was based on the central-difference scheme with  
 50 a scalar dissipation term which is typically more dissipative than the upwind scheme in the explicit operator.  
 51 In contrast, when the dissipation level of the implicit operator is equal to that of the explicit operator, the sta-  
 52 bility can be severely restricted [17]. These observations clearly indicate that it is difficult to construct an effi-  
 53 cient and robust implicit operator by adopting existing numerical splitting schemes with fixed level of  
 54 numerical dissipation.

55 In the present study, a new implicit operator has been developed for the improvement of the efficiency and  
 56 the robustness of the point GS method. For this purpose, an artificial dissipation model with an adjustable  
 57 coefficient was incorporated in the upwind implicit side to flexibly control the dissipation level. Initially,  
 58 the dependency of the stability characteristics on the dissipation level of the implicit operator was examined  
 59 by applying the von Neumann stability analysis to a scalar model equation. Then assessment of the perfor-  
 60 mance of existing implicit operators, which have been widely used for solving the Euler and Navier–Stokes  
 61 equations, was made by testing the effect of their dissipation levels on the stability and convergence charac-  
 62 teristics. Based on the insights from the analyses, an appropriate artificial dissipation model for the implicit  
 63 operator of the point GS method was suggested. Finally, the benefits of using the artificial dissipation model  
 64 in conjunction with upwind schemes were demonstrated through numerical experiments for flows ranging  
 65 from subsonic to hypersonic speeds.

## 66 2. Implicit point Gauss–Seidel method

67 The two-dimensional compressible Euler equations under the ideal gas assumption may be written in an  
 68 integral form for a control volume  $\Omega$  with the boundary  $\partial\Omega$ :

$$69 \quad \frac{\partial}{\partial t} \int_{\Omega} Q \, dV + \oint_{\partial\Omega} f(Q) \, dl = 0, \quad (1)$$

72 where  $Q$  represents the vector of dependent variables, and  $f(Q)$  is the inviscid flux vector. The governing equa-  
 73 tions were discretized using a node-based finite-volume method in which the variables were stored at the nodes  
 74 of the mesh. The computational domain was divided into a finite number of triangles, and the control volumes  
 75 were constructed from the median duals surrounding each node [11]. The application of the Euler implicit  
 76 method and the local time linearization yields a linear system of equations:

$$77 \quad \mathbf{L}\Delta Q^n = -\mathbf{R}, \quad (2)$$

80 where  $\Delta Q^n = Q^{n+1} - Q^n$ .  $\mathbf{L}$  represents the implicit operator constructed with block matrices and has a dimen-  
 81 sion equal to the total number of nodes  $N$ . Also,  $\mathbf{R}$  represents the explicit operator, which is a column vector  
 82 with  $N$  block entries. The explicit and implicit operators for the  $i$ th row are

83

$$\mathbf{R}_i = \sum_{j \in n_f(i)} F_{ij}(Q_L^n, Q_R^n) l_{ij}, \quad (3)$$

85

$$\mathbf{L}_i = \frac{V_i}{\Delta t_i} I + \frac{\partial \mathbf{R}_i}{\partial Q}. \quad (4)$$

86 Here,  $n_f(i)$  is a set of face neighbor nodes for node  $i$ , and  $l_{ij}$  is the length of the control volume boundary shared  
 87 by nodes  $i$  and  $j$ . Also,  $V_i$  is the area of the control volume for node  $i$ . The local time step at node  $i$ ,  $\Delta t_i$ , is  
 88 determined from the definition of the Courant–Friedrichs–Lewy (CFL) number.  $F_{ij}(Q_L^n, Q_R^n)$  is the numerical  
 89 flux vector at the control volume boundary shared by nodes  $i$  and  $j$ , and the subscripts L and R refer to the left  
 90 and right states, respectively. The numerical flux of the explicit operator was evaluated in a second-order accu-  
 91 rate manner using a linear reconstruction method, while the Jacobian  $\partial \mathbf{R}_i / \partial Q$  for the implicit operator was  
 92 approximated to first-order accuracy. This defect correction algorithm [18] has been commonly adopted in  
 93 many implicit flow solvers, because the bandwidth can be reduced and the diagonal dominance property of  
 94 the implicit operator is enhanced.

95 To obtain first-order accuracy, the flow variables at the left and right sides of the control volume boundary  
 96 were set to those of the nodes at each side of the boundary. For second-order accuracy, the primitive variables  
 97 were linearly extrapolated to the control volume boundary using a Taylor series expansion. The solution gra-  
 98 dient required for the expansion was calculated using an unweighted least-square procedure [11]. This second-  
 99 order approach is equivalent to a second-order, upwind-biased MUSCL differencing on Cartesian meshes [19].  
 100 In order to suppress the numerical oscillation of the solution associated with the reconstruction, Venkata-  
 101 krishnan’s limiter [20] was adopted.

102 The solution of the linear system of equations in Eq. (2) can be obtained by using a point Gauss–Seidel  
 103 (GS) method in which several inner iterations with forward and backward sweeps are performed at each time  
 104 step. The implicit matrix operator  $\mathbf{L}$  may be split into three parts:

$$106 \quad \mathbf{L} = \mathbf{D} + \mathbf{T}_1 + \mathbf{T}_2, \quad (5)$$

107 where  $\mathbf{D}$  is the diagonal matrix, and  $\mathbf{T}_1$  and  $\mathbf{T}_2$  are the strictly lower and upper matrices, respectively. Then the  
 108 point GS method can be written as the following two steps [21]:

$$109 \quad [\mathbf{D} + \mathbf{T}_1] \Delta Q^k + [\mathbf{T}_2] \Delta Q^{k-1} = -\mathbf{R}, \quad (6)$$

$$110 \quad [\mathbf{D} + \mathbf{T}_2] \Delta Q^k + [\mathbf{T}_1] \Delta Q^* = -\mathbf{R}. \quad (7)$$

111 The first equation corresponds to the forward sweep and the second one represents the backward sweep. The  
 112 superscript  $k$  ( $k = 1, 2, 3, \dots$ ) refers to the inner iteration index, and the superscript  $*$  denotes the most recent  
 113 values obtained from the forward sweep. The initial value  $\Delta Q^0$  is taken to be zero.

114 Although the point GS method was originally developed for solving unfactored system of equations, it may  
 115 also be expressed in a form equivalent to approximate factorization. Then the factorization error of the point  
 116 GS method can be written as [21]

$$117 \quad AF = [\mathbf{T}_1][\mathbf{D}]^{-1}[\mathbf{T}_2]\Delta Q^n. \quad (8)$$

120 The factorization error is known to be the main source of deteriorating the stability and convergence charac-  
 121 teristics of approximate factorization methods, including the point GS method [21,22].

### 122 3. Analysis of point Gauss–Seidel method

123 In this section, the effect of the numerical dissipation level of the implicit operator on the performance of  
 124 the point GS method was examined by applying the von Neumann stability analysis [5] to an idealized scalar  
 125 model equation. In this stability analysis, the solution was decomposed into a Fourier series as  
 126  $Q_{i,j}^n = E^n e^{i n \phi_x} e^{i j \phi_y}$ , where  $E^n$  is the error amplitude at time level  $n$ , and  $\phi_x$  and  $\phi_y$  are the  $x$ - and  $y$ -directional  
 127 spatial frequencies, respectively. The magnitude of the largest eigenvalue of the amplification matrix defined  
 128 by  $G = E^{n+1}/E^n$  is the amplification factor and is denoted by  $|G|$ .

129 Consider a two-dimensional scalar convection equation

$$131 \quad \frac{\partial}{\partial t} \int_{\Omega} u \, dV + \oint_{\partial \Omega} f(u) \, dl = 0, \quad (9)$$

132 where  $f = (au\hat{i} + bu\hat{j}) \cdot \hat{n}$  and  $\hat{n}$  refers to the unit normal vector pointing outward from the control volume  
 133 boundary. The constants  $a$  and  $b$  are the wave speeds in the  $x$  and  $y$  directions, respectively. Opposite signs  
 134 are assigned to the wave speeds (in the present study,  $a > 0$  and  $b < 0$ ) to account for the eigenvalues with  
 135 mixed signs of the system of equations in Eq. (1). For the wave speeds with same signs, the factorization error  
 136 always cancels out when the relaxation is performed in a symmetric manner, as done in the present study. This  
 137 scalar equation was discretized using the Euler implicit method and the local time linearization as done in Eqs.  
 138 (2)–(4). The spatial accuracy of the implicit operator was set to first order, and the explicit operator was ob-  
 139 tained using a second-order, upwind-biased MUSCL scheme for the Cartesian meshes adopted in this stability  
 140 analysis.

141 A generic form of upwind schemes may be written as

$$143 \quad F_{i+1/2,j} = \frac{1}{2}[au_L + au_R - |a|(u_R - u_L)]. \quad (10)$$

144 Then the first-order accuracy can be achieved by setting the state variables at the left and right sides of the  
 145 control volume boundary as

$$147 \quad u_L = u_{i,j}, \quad u_R = u_{i+1,j}. \quad (11)$$

148 The central-difference scheme with a second-difference artificial dissipation term can also be written in a form  
 149 similar to that of upwind schemes:

$$151 \quad F_{i+1/2,j} = \frac{1}{2}[au_L + au_R - \varepsilon_i|a|(u_R - u_L)], \quad (12)$$

152 where  $\varepsilon_i$  is the parameter which controls the amount of added dissipation.

153 In order to examine the effect of the numerical dissipation level of the implicit operator, the numerical flux  
 154 of the implicit operator is modified by adding the second-difference artificial dissipation to the first-order  
 155 upwind scheme:

$$157 \quad F_{i+1/2,j} = \frac{1}{2}[au_L + au_R - (1 + \varepsilon_i)|a|(u_R - u_L)]. \quad (13)$$

158 Then the Jacobians for the implicit operator become

$$160 \quad \begin{aligned} A_{i+1/2,j}^+ &= \frac{\partial F_{i+1/2,j}}{\partial u_L} = \frac{1}{2}[a + (1 + \varepsilon_i)|a|], \\ A_{i+1/2,j}^- &= \frac{\partial F_{i+1/2,j}}{\partial u_R} = \frac{1}{2}[a - (1 + \varepsilon_i)|a|]. \end{aligned} \quad (14)$$

161 The numerical flux of the explicit operator is not changed, and thus the numerical flux of the implicit operator  
 162 is more dissipative than that of the explicit operator when  $\varepsilon_i > 0$ . For  $\varepsilon_i < 0$ , an opposite statement can be  
 163 made. When  $\varepsilon_i = 0$ , the levels of numerical dissipation in both operators are equal.

164 In Fig. 1, the maximum value of the amplification factor obtained over the entire spatial frequency spec-  
 165 trum is presented as a function of CFL number for selected values of  $\varepsilon_i$ . The results were obtained by perform-  
 166 ing single inner iteration for a flow angle,  $\theta = b/a$ , of  $-10^{-2}$ . The grid aspect ratio,  $AR = dx/dy$ , was set to  
 167 unity since the Euler equations are typically calculated using meshes with nearly isotropic cells. Note that  
 168 for a stable method, the value of the maximum amplification factor is unity, since the amplification factor  
 169 at the lowest spatial frequency mode (i.e.,  $\phi_x = \phi_y = 0$  mode) is always unity.

170 When  $\varepsilon_i = -0.5$ , the point GS method becomes unstable for CFL numbers higher than unity. This limiting  
 171 CFL number increases to approximately 10 when the dissipation levels in both operators are equal (i.e.,  
 172  $\varepsilon_i = 0$ ). As the dissipation level of the implicit operator further increases, the unstable behavior is rapidly alle-  
 173 viated, indicating that the stability characteristics of the point GS method can be improved by increasing the  
 174 dissipation level of the implicit operator. However, with excessive dissipation, even though the method  
 175 becomes unconditionally stable, the amplification factor approaches unity for all spatial frequencies and  
 176 the convergence rate can deteriorate considerably. The results imply that the stability and convergence char-  
 177 acteristics of the point GS method can be improved simultaneously only when the numerical dissipation level  
 178 of the implicit operator is properly adjusted, presumably higher than that of the explicit operator. It was

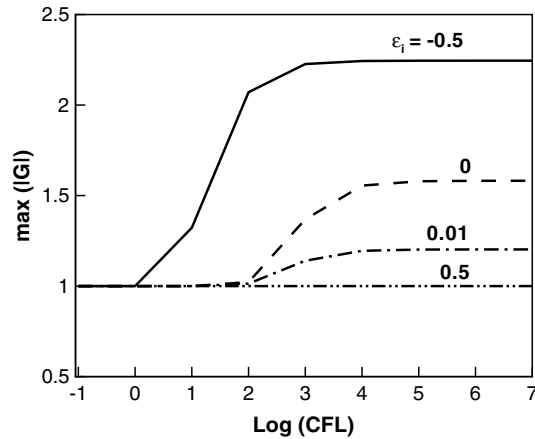


Fig. 1. Maximum amplification factor obtained over the entire spatial frequency spectrum as a function of CFL number for selected values of  $\varepsilon_i$  (scalar equation).

179 observed that at other flow conditions with different flow angles or number of inner iterations, the essential  
180 features of the analysis were unchanged.

181 In principle, the convergence of the inner iteration procedure for the point GS method can be assured when  
182 the implicit operator is diagonally dominant. For first-order accurate upwind schemes, the diagonal domi-  
183 nance is always guaranteed for any time step size [23]. When the second-difference artificial dissipation is  
184 added to the upwind schemes, the ratio of the magnitude of the diagonal element to the sum of the magnitudes  
185 of the off-diagonal elements can be written as  
186

$$188 \quad 1 + \frac{V_{i,j}/\Delta t_{i,j}}{2(1 + \varepsilon_i)(a \, dy - b \, dx)}. \quad (15)$$

189 It shows that when the magnitude of  $\varepsilon_i$  increases above zero, the diagonal dominance of the implicit operator is  
190 degraded and as a result the convergence rate of the inner-iteration procedure deteriorates. This indicates that  
191 for the efficiency and the robustness of the upwind point GS method, the added artificial dissipation should  
192 not be too large.

#### 193 4. Existing implicit operators

194 Implicit operators can be obtained by applying the local time linearization to numerical fluxes. Consistent  
195 upwind (CU) implicit operators are constructed by adopting same upwind schemes for both explicit and impli-  
196 cit operators [1,15,16,24]. Alternatively, central-difference schemes can also be used in the implicit operator,  
197 while the explicit operator still employs an upwind scheme. For the central-difference schemes, the diagonal  
198 dominance property can be achieved only for a very small time step size, rendering the point GS method inef-  
199 ficient. Nevertheless, Jameson and Turkel [25] showed that a diagonally dominant central-difference implicit  
200 operator can still be constructed by adding numerical dissipation.

##### 201 4.1. Construction of implicit operators

202 The upwind numerical flux vector based on Roe's flux-difference splitting (FDS) scheme [26] can be written  
203 at the control volume boundary shared by nodes  $i$  and  $j$  as  
204

$$206 \quad F_{ij} = \frac{1}{2} [f(Q_L) + f(Q_R) - |A(\tilde{Q})|(Q_R - Q_L)], \quad (16)$$

207 where the flux Jacobian matrix  $A$  is defined by  $A = \partial f / \partial Q$ .  $\tilde{Q}$  represents the Roe-averaged values of the left and  
208 right states. Then the Jacobian matrices are obtained by linearizing the numerical flux in Eq. (16):

6

*J.S. Kim, O.J. Kwon / Journal of Computational Physics xxx (2006) xxx–xxx*

209

$$A_{ij}^+ = \frac{1}{2}[A(Q_L) + |A(\tilde{Q})|], \quad A_{ij}^- = \frac{1}{2}[A(Q_R) - |A(\tilde{Q})|]. \quad (17)$$

212 In the linearization process,  $|A(\tilde{Q})|$  is frozen in time [1].

213 The central-difference scheme with a second-difference scalar dissipation term can be written as

$$F_{ij} = \frac{1}{2}[f(Q_L) + f(Q_R) - k|\rho|(Q_R - Q_L)], \quad (18)$$

216 where  $k$  is a constant to be specified and  $|\rho|$  is the spectral radius of the flux Jacobian matrix. The Jacobian  
217 matrices of the Jameson–Turkel (JT) implicit operator are obtained by linearizing the central-difference  
218 scheme [27]:

$$A_{ij}^+ = \frac{1}{2}[A(Q_L) + |\rho|I], \quad A_{ij}^- = \frac{1}{2}[A(Q_R) - |\rho|I], \quad (19)$$

222 where the constant  $k$  is suppressed because it is typically set to unity.

223 Since the Euler equations are hyperbolic, the flux Jacobian matrix  $A$  can be diagonalized. Then  $|A|$  can be  
224 written as  $|A| = P|A|P^{-1}$ , where the columns of the matrix  $P$  consist of the right eigenvectors of  $A$ . The diag-  
225 onal matrix  $|A|$  is given by  $|A| = \text{Diag}[|\lambda_1|, |\lambda_2|, |\lambda_3|, |\lambda_4|]$ , where  $\lambda_i$ 's are the eigenvalues of  $A$ . Then the coeffi-  
226 cient in the dissipation term of the central-difference scheme can be written as a linear combination of two  
227 matrices:

$$|\rho|I = P|\rho|P^{-1} = |A| + A_{JT}, \quad (20)$$

230 where

$$A_{JT} = PA_{JT}P^{-1}, \quad (21)$$

$$A_{JT} = \text{Diag}[|\rho| - |\lambda_1|, |\rho| - |\lambda_2|, |\rho| - |\lambda_3|, |\rho| - |\lambda_4|]. \quad (22)$$

233 It is clear that every element of  $A_{JT}$  is greater than or equal to zero, because the spectral radius  $|\rho|$  is defined by  
234 the largest eigenvalue of the matrix  $A$ . When the spectral radius is evaluated based on the Roe-averaged val-  
235 ues, the Jacobian matrices of the JT implicit operator in Eq. (19) can be rewritten as

$$A_{ij}^+ = \frac{1}{2}[A(Q_L) + (|A(\tilde{Q})| + A_{JT}(\tilde{Q}))], \quad (23)$$

$$A_{ij}^- = \frac{1}{2}[A(Q_R) - (|A(\tilde{Q})| + A_{JT}(\tilde{Q}))].$$

239 Compared to the upwind implicit operator based on Roe's FDS scheme in Eq. (17), the Jacobian matrices of  
240 the JT implicit operator contain an additional positive dissipation term. Thus, it is evident that the JT implicit  
241 operator is more dissipative than the upwind implicit operator.

#### 242 4.2. Numerical experiments of existing implicit operators

243 The numerical behavior of the two implicit operators were examined through numerical experiments, with  
244 an emphasis on the effect of the numerical dissipation level of the operators. The selected test case was the flow  
245 over a solid bump described by  $y = t \sin^2(\pi x)$  and located at  $0 \leq x \leq 1$  [28]. For a fixed free stream Mach num-  
246 ber of 0.8, two different flow problems, fully subsonic and transonic, were computed by changing the bump  
247 thickness  $t$ . The overall computational domain was 20 unit lengths long and 10 unit lengths high. The domain  
248 was decomposed into an unstructured triangular mesh composed of 6359 nodes, of which 215 lied on the  
249 bump surface. The slip boundary condition was imposed at the bottom boundary of the computational  
250 domain, including the bump. The characteristic boundary condition was applied to three other boundaries.  
251 In the explicit operator, Roe's FDS scheme was adopted.

252 In Fig. 2, the Mach number contours for 2% and 20% thick bumps are presented. It shows that the flow  
253 field of the 2% thick bump is completely subsonic, whereas for the 20% thick bump a strong shock wave exists  
254 at the leeward of the bump.

255 In Fig. 3, the convergence histories of the CU and JT implicit operators are compared for the bump flows.  
256 The convergence was measured by taking the logarithm of the  $L_2$  norm of the residual of the conservation-of-

257 mass equation. In the beginning of the calculation, the CFL number was set to one for all test cases, and then  
258 increased inversely proportional to the reduction of the  $L_2$  norm up to  $10^7$  or until the maximum allowable  
259 value was reached. For the 2% thick bump flow, both CU and JT implicit operators were stable for all  
260 CFL numbers tested. However, the CU operator led to a much better convergence rate than the JT operator,  
261 indicating that addition of more dissipation to the implicit operator simply degrades the convergence behavior  
262 for fully subsonic flows.

263 In contrast, the results for the 20% thick bump flow revealed that the CU implicit operator is under a severe  
264 stability restriction, and the maximum allowable CFL number to obtain a machine-accurate solution was as low  
265 as three. However, the JT implicit operator did not suffer any stability restriction for all CFL numbers tested and  
266 led to a better convergence rate. The results of this 20% thick bump flow involving a strong shock wave indicated  
267 that the stability characteristics improve as the dissipation level of the implicit operator increases.

268 When the maximum CFL number was set to 30 for the flow over the 20% thick bump, the calculation using  
269 the CU implicit operator failed after 103 iterations. In Fig. 4, contours of the density residual are presented  
270 after 100 iterations, just before the calculation started to diverge. It clearly revealed that the region of signif-  
271 icantly large residual values appears near the shock wave, indicating that the numerical instability of the CU  
272 implicit operator is intimately related to the presence of a strong solution gradient such as the shock wave.  
273 From the above stability and convergence results, it was found that the CU implicit operator in general  
274 has non-robust numerical behaviors, while the JT implicit operator is very robust but may lead to slow con-  
275 vergence. As a consequence of these results, it is highly desirable to devise a new implicit operator that is both  
276 efficient and robust for calculating flows involving strong solution gradients by properly adjusting the amount  
277 of added dissipation depending on the local flow characteristics.

## 278 5. Implicit operator with added artificial dissipation (AD)

279 It was shown that for the robustness of the point GS method, the numerical flux of the implicit operator  
280 needs to be more dissipative than that of the explicit operator. To achieve this feature, additional artificial dis-

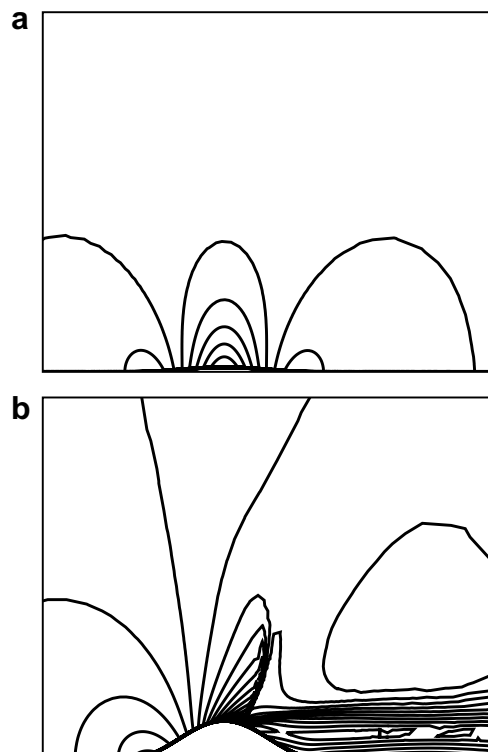


Fig. 2. Mach number contours over the bump: (a) 2% thickness and (b) 20% thickness.

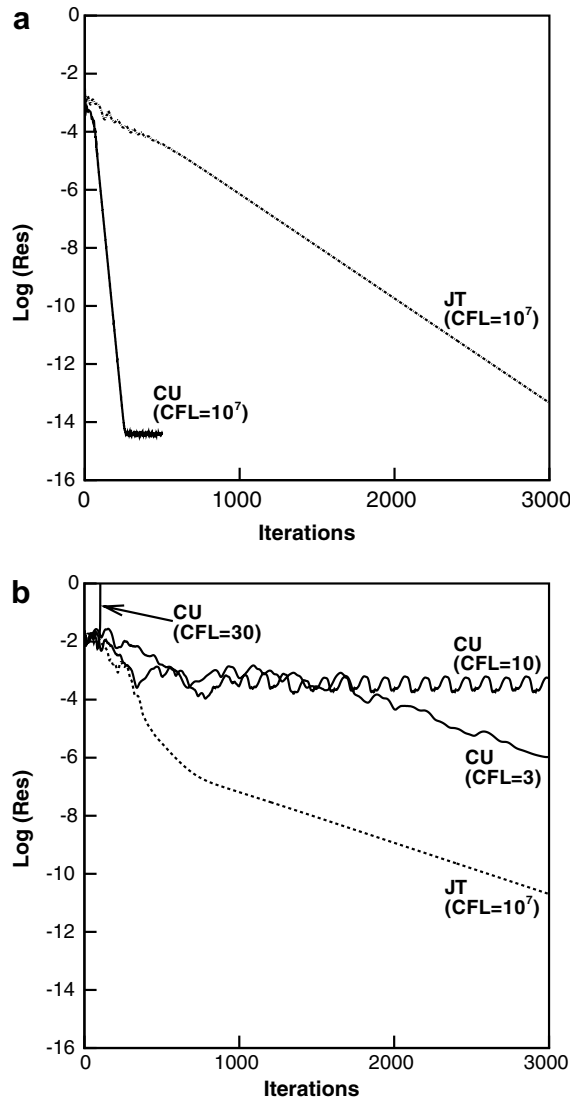


Fig. 3. Comparison of convergence histories between the CU and JT implicit operators for the bump flow: (a) 2% thickness and (b) 20% thickness.

281 sipation can be added to the implicit operator. The concept of adding artificial dissipation to the upwind impli-  
 282 cit side was first attempted by Strang et al. [29] for the enhancement of the diagonal dominance. However, the  
 283 addition of artificial dissipation in fact has an effect of deteriorating the diagonal dominance of the implicit  
 284 operator, as shown in the previous section. In the present study, a second-difference artificial dissipation term  
 285 was added to the upwind implicit side to increase the amount of dissipation of the implicit operator. Then the  
 286 Jacobian matrices of the new implicit operator (AD) based on the numerical flux of Roe's FDS scheme can be  
 287 written as

$$A_{ij}^+ = \frac{1}{2} [A(Q_L) + (|A(\tilde{Q})| + \beta|\rho|)], \quad (24)$$

$$A_{ij}^- = \frac{1}{2} [A(Q_R) - (|A(\tilde{Q})| + \beta|\rho|)],$$

289



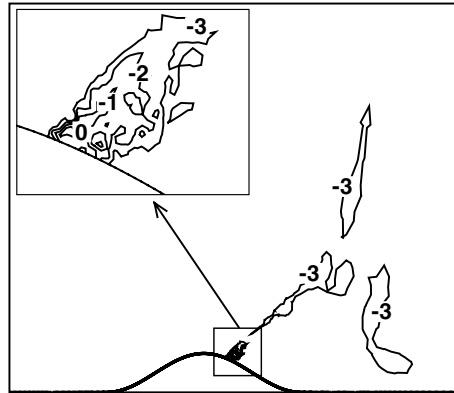


Fig. 4. Contours of the logarithm of the density residual just before the calculation started to diverge for the 20% thick bump flow.

where the coefficient  $\beta$  is used to control the amount of added dissipation. Note that in the present AD implicit operator, a scalar form of artificial dissipation is added to the CU implicit operator, while the JT implicit operator in Eq. (23) has a matrix form.

To achieve fast convergence while maintaining good stability simultaneously, it is essential to choose  $\beta$  properly. In the present study,  $\beta$  was determined based on the von Neumann linear stability analysis such that the present AD implicit operator has the stability characteristics equivalent to those of the robust JT operator. For a demonstration purpose, the stability characteristics of the existing CU and JT operators were examined for the linearized constant coefficient Euler equations. The results were obtained at a Mach number of 0.3, and the flow angle, the grid aspect ratio, and the number of inner iteration were set equal to those used for the analysis of the scalar equation in Fig. 1. The CFL number was set to  $10^7$ . In the explicit operator, a second-order accurate upwind biased scheme was used. In Fig. 5, contours of the amplification factor of the CU and JT implicit operators are presented. It shows that while both implicit operators are unstable at low spatial frequencies, the maximum amplification factor of the JT implicit operator was still less than that of the CU operator, confirming that the JT operator is more robust than the CU operator.

In Fig. 6, the values of  $\beta$  which yield the maximum amplification factor of the AD implicit operator equivalent to that of the JT operator are presented for various flow angles and Mach numbers. The flow angle changed from 0 to 1 in radian, and the local Mach number was tested between 0.2 and 5. The face Mach number  $M_{\text{face}}$  was defined by the normal component of the local Mach number at the control volume face. The results were obtained for a fixed CFL number of  $10^7$  by performing single inner iteration on an isotropic grid. From the results, it was found that the AD implicit operator has stability characteristics similar to or less than those of the JT operator, independent to the Mach number and the flow angle, when the coefficient  $\beta$  is determined as a function of the face Mach number

$$\beta = \frac{b}{\max(1, M_{\text{face}})}, \quad (25)$$

where the value of  $b$  is approximately 0.7.

In Fig. 7, contours of the amplification factor of the AD implicit operator are presented for the same flow condition in Fig. 5. It shows that the damping characteristics of the AD implicit operator are very similar to those of the JT operator in Fig. 5b over most of the spatial frequency spectrum, demonstrating that the stability and convergence characteristics of the AD implicit operator are very comparable to those of the JT operator.

In order to further improve the convergence characteristics of the AD implicit operator, the amount of added dissipation is adaptively adjusted depending on the flow characteristics. This technique is based on the observation that the instability of the CU implicit operator is mostly associated with large solution gradients such as the shock wave and thus the added dissipation is needed only in the local stiff flow regions. This adjustment can be made by imposing a weighting to the added dissipation based on the magnitude of the solution gradients, similar to the adaptive artificial dissipation for central-difference schemes [2]. An effective

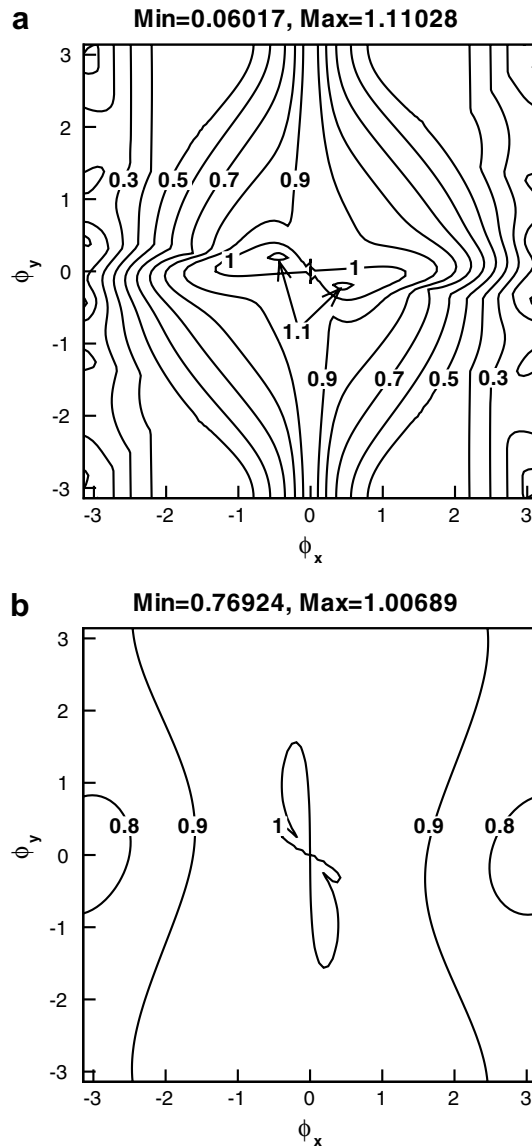


Fig. 5. Contours of the amplification factor: (a) CU implicit operator and (b) JT implicit operator.

327 choice of the weighting factor at the control volume face is the normalized second-difference of pressure [2],  
 328 and for unstructured meshes this weighting factor can be evaluated using the undivided Laplacian of pressure  
 329 [30]:

$$\tau_{ij} = \max(\tau_i, \tau_j), \quad (26)$$

$$\tau_i = \frac{|\sum_{k \in n_f(i)} (p_k - p_i)|}{\sum_{k \in n_f(i)} (p_k + p_i)}. \quad (27)$$

332 Then the AD implicit operator can be written as

$$A_{ij}^+ = \frac{1}{2} [A(Q_L) + (|A(\tilde{Q})| + \tau\beta|\rho|)], \quad (28)$$

$$334 \quad A_{ij}^- = \frac{1}{2} [A(Q_R) - (|A(\tilde{Q})| + \tau\beta|\rho|)].$$

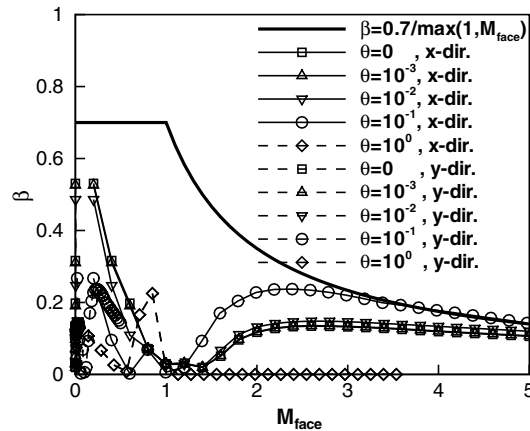


Fig. 6. Values of added dissipation coefficient  $\beta$  needed for the AD implicit operator to yield the maximum amplification factor equivalent to that of the JT operator.

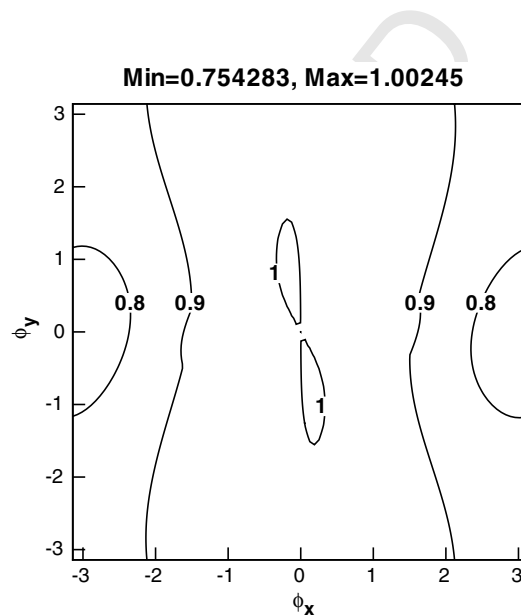


Fig. 7. Contours of the amplification factor of the AD implicit operator.

335 In the region of smooth flow,  $\tau$  is proportional to the square of the cell size, and thus the effect of the added  
 336 dissipation becomes negligible. When strong pressure gradients exist, the order of  $\tau$  increases and the added  
 337 dissipation works effectively for stabilizing the calculation. Here, the value of the constant  $b$  in Eq. (25) needs  
 338 to be adjusted properly because  $\tau$  is not unity in the region where the added dissipation is in effect. For practical  
 339 calculations of flows ranging from subsonic to hypersonic speeds, a reasonable value of  $b$  is unity. This  
 340 value was used for all numerical experiments presented in the next section. Adaptive control of the added  
 341 dissipation also reduces the degradation of the diagonal dominance of the implicit operator, which is inevitably  
 342 caused by the addition of the artificial dissipation to the upwind implicit operator as shown in Eq. (15).

343 For Cartesian meshes, when the velocity component normal to all control volume faces is supersonic, the  
 344 CU implicit operator is not subject to any approximate factorization error. This is because either one of the  
 345 lower matrix  $\mathbf{T}_1$  or the upper matrix  $\mathbf{T}_2$  in Eq. (8) becomes zero. In contrast, since the spectral radius is used in  
 346 the coefficient of the dissipation term, the JT implicit operator does not have this favorable property. Even  
 347 though this is true only for Cartesian meshes, the approximate factorization error of the CU implicit operator

348 is also expected to be smaller than that of the JT operator even on unstructured meshes. Since the present AD  
 349 implicit operator is constructed such that the added dissipation becomes active locally in the neighborhood of  
 350 stiff flow regions and it recovers to the CU implicit operator for the rest of the flow field, the magnitude of the  
 351 approximate factorization error of the AD implicit operator is approximately equivalent to that of the CU  
 352 operator.

353 The AD implicit operator can also be constructed for any other upwind numerical fluxes in a similar man-  
 354 ner by adding the artificial dissipation to the corresponding Jacobian matrices.

## 355 6. Numerical results

356 Several compressible flows ranging from subsonic to hypersonic speeds were calculated to examine the sta-  
 357 bility and convergence characteristics of the three implicit operators for practical nonlinear problems. The  
 358 numerical experiments about the effect of meshes with varying density were also conducted using solution-  
 359 adaptive local mesh refinement based on the second derivative of density [31]. For the upwind differencing

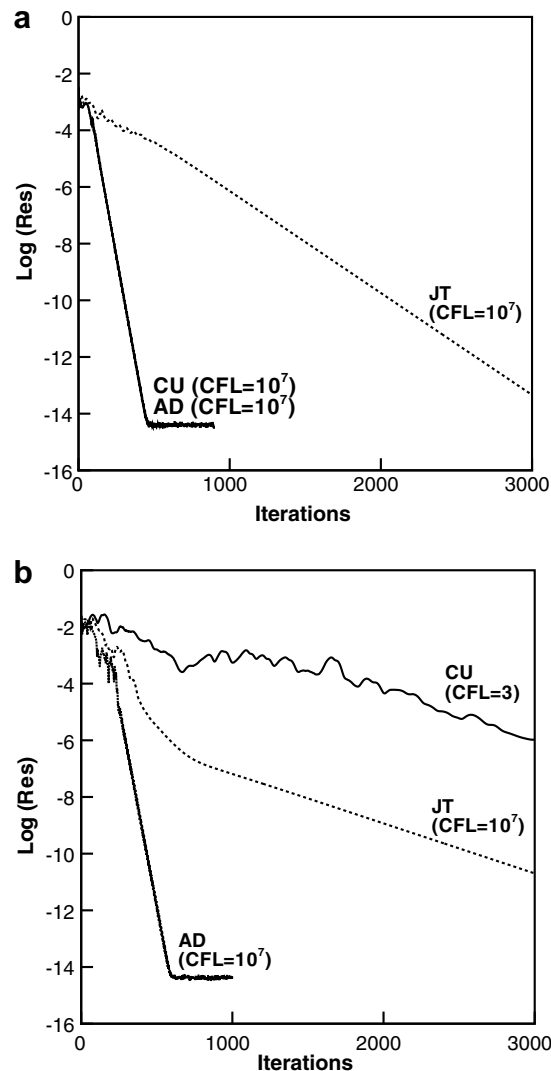


Fig. 8. Comparison of convergence histories of the three implicit operators for the bump flow: (a) 2% thickness and (b) 20% thickness.

360 of the nonlinear flux term, Roe's FDS scheme was mostly used, but van Leer's flux-vector splitting (FVS)  
 361 scheme [32] was also tested to confirm the robustness of the present AD implicit operator. In these numerical  
 362 experiments, the number of inner iterations was fixed to 10 for all test cases to maintain the consistency of the  
 363 analysis, even though the implicit operators were not at the maximum performance. The CFL number ranged  
 364 from 1 to  $10^7$  and was increased inversely proportional to the reduction of the  $L_2$  norm of the residual.

### 365 6.1. Bump flow

366 At first, the bump flow tested for the assessment of the performance of the existing operators was adopted  
 367 again for numerical experiment. The convergence histories of the three implicit operators are compared in  
 368 Fig. 8 for the maximum allowable CFL number of each operator above which the calculation simply diverges  
 369 or enters into a limited cycle oscillation after a few orders of residual reduction. Even though the best conver-  
 370 gence rate was obtained at a CFL number slightly lower than the maximum allowable CFL number [33], the  
 371 convergence results are shown for the maximum allowable CFL number since the difference is relatively small.

372 For the 2% thick bump flow, the stability and convergence characteristics of the AD implicit operator were  
 373 similar to those of the CU operator. Since the amount of dissipation added to the AD implicit operator was  
 374 monitored by the magnitude of the pressure gradient, the numerical behavior of the AD implicit operator was  
 375 evidently almost identical to that of the CU operator for this pure subsonic flow. It shows that all implicit  
 376 operators considered were stable up to the largest CFL number tested, but the CU and AD implicit operators  
 377 exhibited much better convergence rates than the JT operator.

378 For the 20% thick bump flow involving a strong shock wave, the CU implicit operator was subject to a  
 379 severe restriction on the CFL number and led to a very slow convergence rate. However, the JT and AD impli-  
 380 cit operators were unconditionally stable, demonstrating the effectiveness of adding numerical dissipation for

Table 1  
Measure of relative CPU time required for the evaluation of each component

Component	Normalized time
Explicit operator	1.0
CU implicit operator	3.56
JT implicit operator	2.85
AD implicit operator	3.59
GS sweeps	14.0

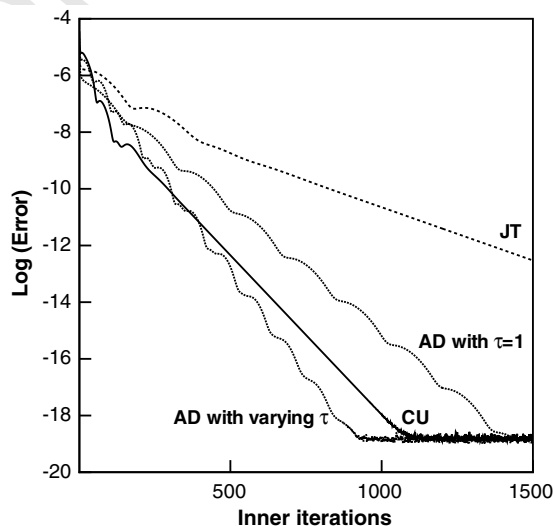


Fig. 9. Comparison of inner-iteration convergence histories of the three implicit operators for the 20% thick bump flow.

381 the improvement of the stability characteristics. Even though the two implicit operators showed similar sta-  
 382 bility characteristics, the AD implicit operator converged much faster than the JT operator.

383 In Table 1, the relative CPU time required for the evaluation of each component of the calculation is pre-  
 384 sented. The CPU time was measured on a PC with Pentium IV 2.4 GHz processor and was normalized by the  
 385 cost for the explicit operator evaluation. It shows that the computational overhead for the evaluation of the  
 386 added dissipation term in the present AD implicit operator was almost negligible compared to the overall

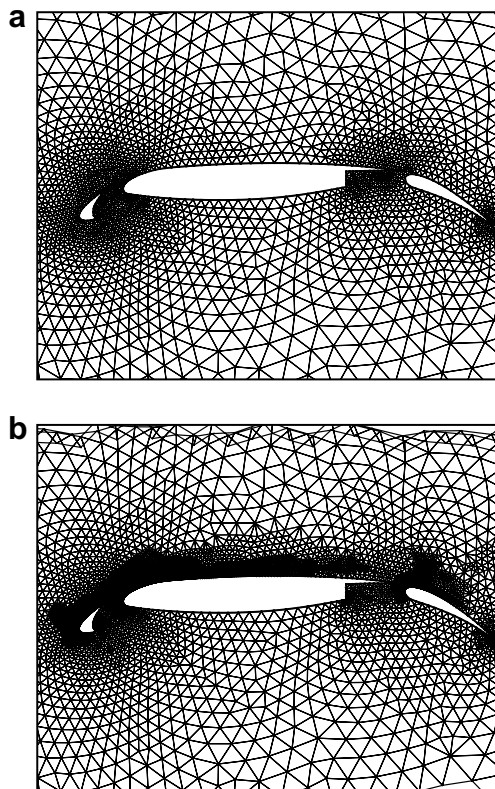


Fig. 10. Partial view of meshes for Douglas three-element airfoil: (a) initial mesh and (b) refined mesh.

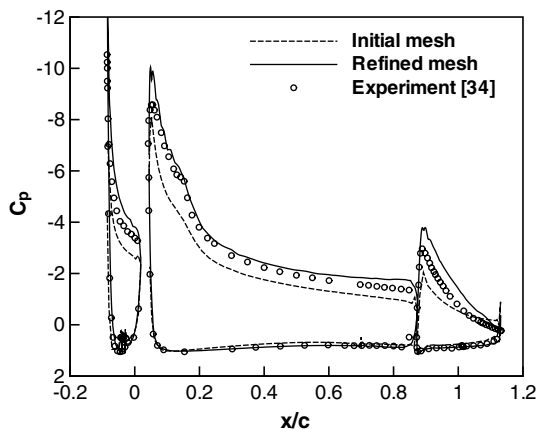


Fig. 11. Comparison of calculated and experimental pressure distributions for Douglas three-element airfoil.

387 computational time. In the case of the subsonic flow, to achieve six orders of residual drop of the  $L_2$  norm, the  
 388 CU and AD implicit operators required 5582 and 5589 normalized CPU time, respectively, while it took  
 389 35,504 for the JT operator. For the transonic flow case, to reach the same level of residual drop, the AD impli-  
 390 cit operator required 6581 normalized CPU time, but the JT and CU operators took 22,437 and 70,435,  
 391 respectively.

392 To examine the effect of added artificial dissipation on the diagonal dominance property of the AD implicit  
 393 operator, the inner-iteration convergence histories are compared for the 20% thick bump flow in Fig. 9. The  
 394 convergence was measured by taking the logarithm of the  $L_2$  norm of the error defined by  $\Delta Q^k - \Delta Q^{k-1}$  where  
 395  $k$  refers to the inner-iteration index. The result for each operator is shown for a CFL number of  $10^7$  after  
 396 restarting from the same intermediate solution obtained after 300 iterations using the AD implicit operator.  
 397 The effect of the adaptive adjustment of the artificial dissipation in the AD implicit operator was also tested by  
 398 comparing the results with those obtained by fixing the weighting factor to unity over the entire computational  
 399 domain as done in [29]. It shows that uniformly added dissipation yielded a slower inner-iteration convergence

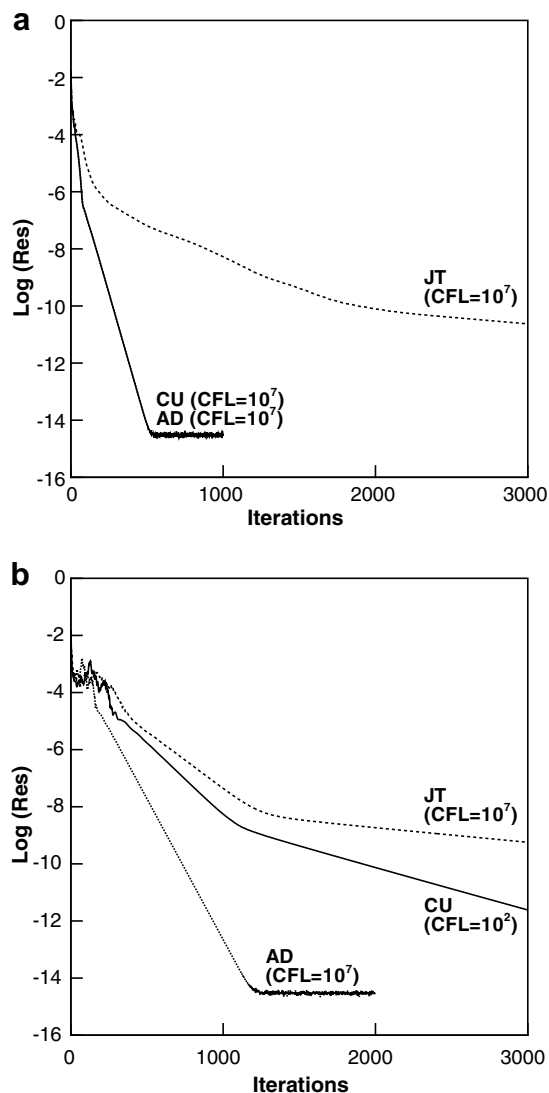


Fig. 12. Comparison of convergence histories of the three implicit operators for Douglas three-element airfoil: (a) initial mesh and (b) refined mesh.

400 rate than the original CU operator, demonstrating that addition of the artificial dissipation in the upwind  
 401 implicit operator deteriorates the diagonal dominance. In contrast, adaptive application of the artificial dissi-  
 402 pation in the vicinity of the shock wave reduced the instability, and thus slightly improved the inner-iteration  
 403 convergence behavior over the CU operator. The JT implicit operator led to the worst inner-iteration perfor-  
 404 mance, presumably due to its excessively dissipative property.

405 In smooth flow regions, because the value of the weighting factor  $\tau$  approaches zero, the CU and AD oper-  
 406 ators become almost identical, and thus the AD operator provides good damping characteristics over the JT  
 407 operator for high frequency modes as shown for the CU operator in Fig. 5. This is a desirable property of a  
 408 good smoother for multigrid schemes. Since the present AD implicit operator shows a much better conver-  
 409 gence behavior than the other two operators for transonic flows, it is expected that the AD implicit operator  
 410 also performs well as a smoother for multigrid schemes even in stiff flow regions.

## 411 6.2. Three-element airfoil flow

412 The second validation was made for a subsonic flow around the Douglas three-element airfoil at a free-  
 413 stream Mach number of 0.2 and an angle of attack of  $16.21^\circ$ . Calculation started on an initial mesh consisted  
 414 of 3015 nodes, of which 174 nodes were on the airfoil surface. To test the effect of mesh density, solution-adap-  
 415 tive mesh refinement by three levels was made, and the size of the final mesh increased to 12,984 nodes with  
 416 571 on the airfoil surface. The initial and final meshes in Fig. 10 show that the mesh refinement was made  
 417 mainly around the airfoil surface and along the wakes emanating from the trailing edge of each element.

418 The calculated surface pressure distributions on the initial and refined meshes are compared with experi-  
 419 mental data [34] in Fig. 11. It shows that the results obtained on the refined mesh generally compare better  
 420 with the experiment than those of the initial mesh, even though the peak values near the leading edge of each  
 421 element were slightly overpredicted, presumably due to the absence of the physical diffusion in the present  
 422 calculation.

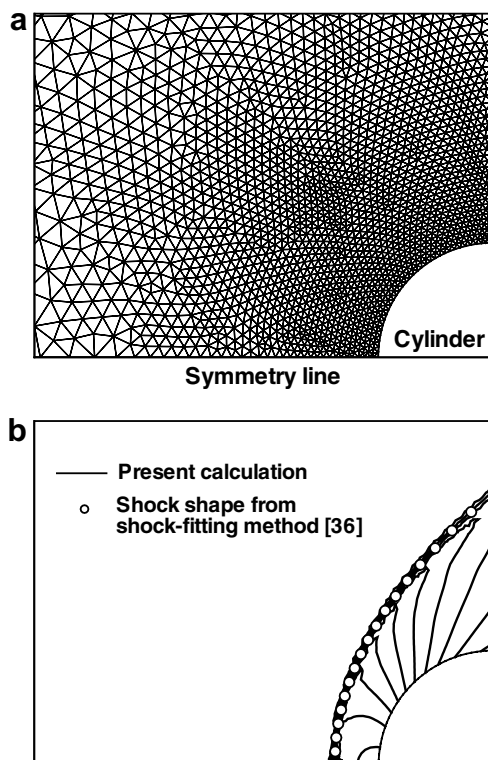


Fig. 13. Supersonic flow past a circular cylinder: (a) partial view of mesh (b) pressure contours at  $M_\infty = 20$ .



423 The convergence histories of the three implicit operators are compared in Fig. 12 on both initial and refined  
 424 meshes for the maximum allowable CFL number of each implicit operator. The CU implicit operator showed  
 425 a stable behavior on the initial mesh up to the largest CFL number tested, but became unstable for CFL num-  
 426 bers above  $10^2$  on the refined mesh. In contrast, the JT and AD implicit operators exhibited an uncondition-  
 427 ally stable behavior on both meshes. This behavior confirmed that the dissipation added in the JT and AD  
 428 implicit operators is effective in increasing the stability limit even for subsonic flows. The dissipation adap-  
 429 tively adjusted based on the pressure gradient in the AD implicit operator worked well also for subsonic flows,  
 430 leading to a much better convergence rate than the CU and JT operators, regardless of the mesh density.

### 431 6.3. Supersonic flow past a circular cylinder

432 The final validation was made for supersonic flows past a circular cylinder at freestream Mach numbers of  
 433 2, 5, 10, 15, and 20. For freestream Mach numbers higher than 10, the entropy correction function [35] was  
 434 employed for both implicit and explicit operators to avoid the carbuncle problem of Roe's FDS scheme. The  
 435 mesh used for the present calculations consisted of 2301 nodes, of which 34 lied on the cylinder surface. The  
 436 computational domain was 5 unit lengths long and 10 unit lengths high. In Fig. 13, a partial view of the mesh  
 437 and the pressure contours at a freestream Mach number of 20 are presented. It shows that the results of the  
 438 present calculation agree well with the prediction by a shock-fitting method [36].

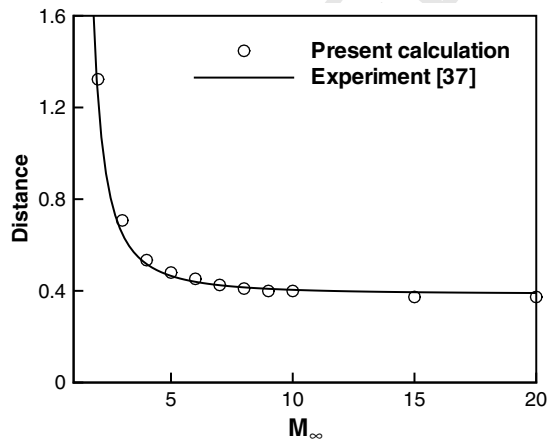


Fig. 14. Shock stand-off distance for supersonic flow past a circular cylinder.

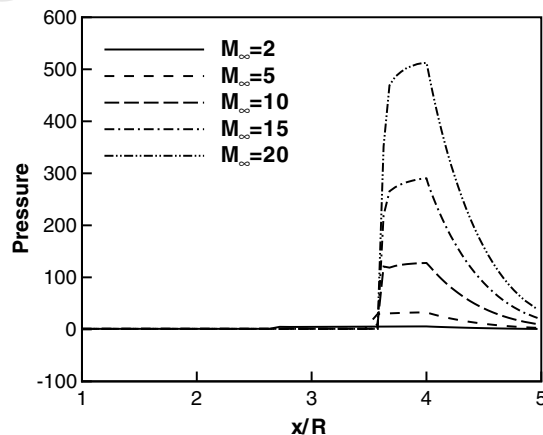


Fig. 15. Pressure distributions along the symmetry line and on the cylinder surface for supersonic flow past a circular cylinder.

In Fig. 14, the calculated shock stand-off distance from the surface of the circular cylinder is compared with experimental data [37]. It shows that the results of the present calculation obtained under the ideal gas assumption agree well with the experimental data. In Fig. 15, the pressure distributions along the symmetry line and on the cylinder surface are compared for all freestream Mach numbers considered. As the freestream Mach number becomes higher, the pressure ratio across the shock wave increases, leading to a large solution gradient.

In Table 2, a summary of the stability and convergence results is presented. Even though the CU implicit operator performed fairly well at  $M_\infty = 2$ , the stability and convergence characteristics rapidly degraded for higher Mach numbers and the maximum allowable CFL number was restricted below 10. This behavior agreed well with other numerical results [24] based on supersonic flows past a rounded cone calculated on structured meshes. For  $M_\infty \geq 10$ , unlike the subsonic and transonic flow cases, the JT implicit operator also

Table 2

Maximum allowable CFL number and the number of iterations required for six orders of residual drop for supersonic flow past a circular cylinder

$M_\infty$	CU		JT		AD	
	CFL	Iterations	CFL	Iterations	CFL	Iterations
2	$10^7$	223	$10^7$	577	$10^7$	280
5	$10^1$	935	$10^7$	514	$10^7$	430
10	5	697	5	1280	$10^7$	302
15	2	2032	3	1406	$10^7$	271
20	2	1941	3	1423	$10^7$	304

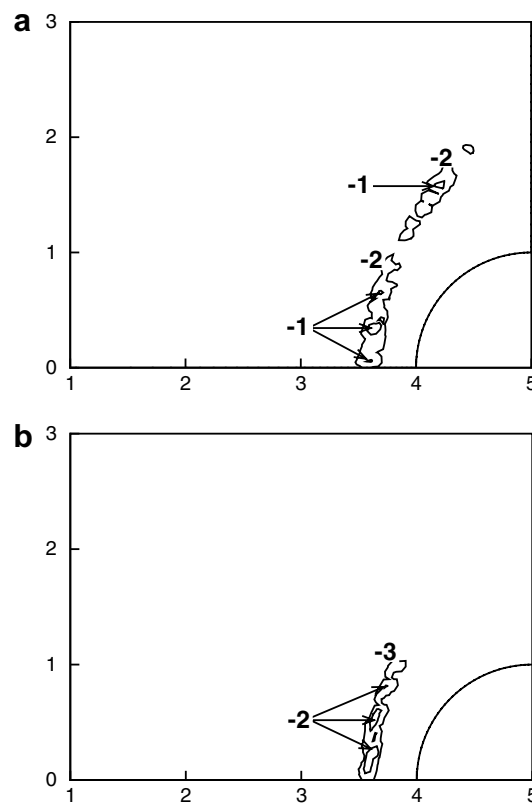


Fig. 16. Contours of the logarithm of the density residual for supersonic flow past a circular cylinder at  $M_\infty = 20$ : (a) CU implicit operator and (b) JT implicit operator.

450 experienced a severe stability restriction, and thus the convergence rate also became significantly poorer. How-  
 451 ever, the AD implicit operator with adaptive artificial dissipation was not subject to any instability for the  
 452 complete range of CFL numbers tested and led to fast convergence rates for all Mach numbers considered.  
 453 From these results, it can be stated that the scalar form of added dissipation employed in the AD implicit  
 454 operator is more effective in alleviating the stability limit than the matrix form of the JT operator, particularly  
 455 for high Mach number flows, even though the numerical behaviors of the two operators by the linear stability  
 456 analysis were similar.

457 In the case of the CU and JT implicit operators, the calculations failed to converge to machine accuracy or  
 458 diverged when the CFL number was set beyond the maximum allowable value depicted in Table 2. In Fig. 16,  
 459 contours of the density residual by the CU and JT implicit operators are presented when the calculation failed  
 460 to converge after a few orders of residual drop for a CFL number of 50. It shows that large residual and flow  
 461 oscillation mostly exist along the shock wave. When the CFL number further increased, the oscillation was  
 462 magnified and the calculation eventually diverged. However, the AD implicit operator was unconditionally  
 463 stable for the complete range of CFL numbers tested.

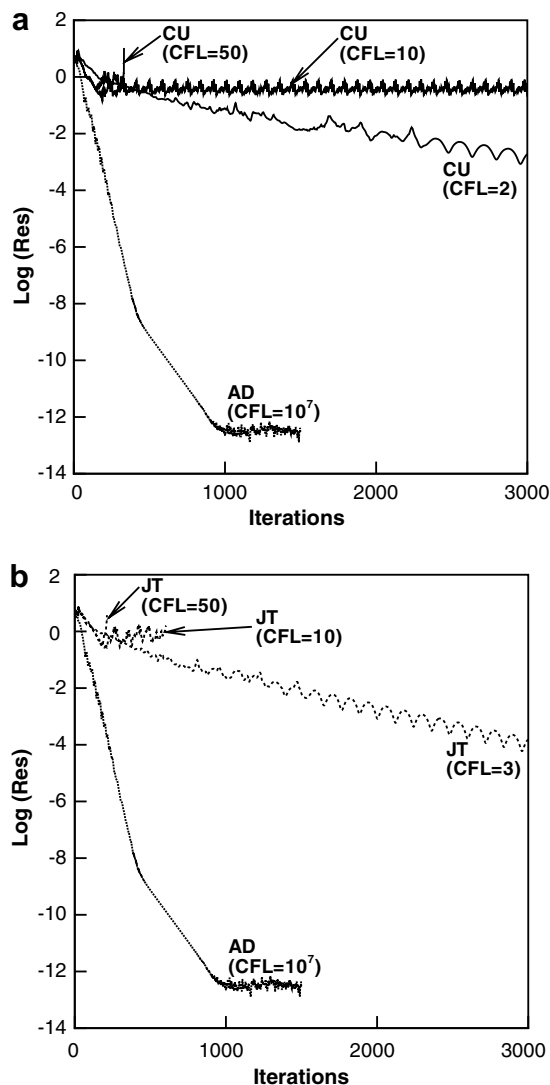


Fig. 17. Comparison of convergence histories on the refined mesh for supersonic flow past a circular cylinder at  $M_\infty = 20$ : (a) CU and AD implicit operators and (b) JT and AD implicit operators.

Table 3

Maximum allowable CFL number and the number of iterations required for six orders of residual drop for supersonic flow past a circular cylinder using van Leer's FVS scheme

$M_\infty$	CU		JT		AD	
	CFL	Iterations	CFL	Iterations	CFL	Iterations
2	$10^7$	205	$10^7$	375	$10^7$	215
5	$10^7$	183	$10^7$	234	$10^7$	203
10	$10^1$	388	$10^1$	430	$10^7$	201
15	5	884	5	958	$10^7$	255
20	5	788	5	840	$10^7$	291

In Fig. 17, the convergence histories on the adaptively refined mesh are presented at a freestream Mach number of 20. The mesh refinement was made mostly along the shock wave and the number of nodes increased to 3251. The results show that the numerical instabilities of the CU and JT implicit operators further amplified on the refined mesh, and the calculations diverged even for very low CFL numbers where on the coarse initial mesh only convergence stall was observed. The AD implicit operator, however, did not show any indication of stability restriction up to the largest CFL number tested and converged very fast on the refined mesh.

The stability and convergence characteristics of the three implicit operators were also tested by adopting van Leer's FVS scheme in the explicit operator, and the results are presented in Table 3. In these calculations, the CU and AD operators were also constructed based on the same FVS scheme. It shows that the AD implicit operator was not subject to any instability and consistently led to good convergence rates at all Mach numbers, while the other two implicit operators were under severe stability restrictions at high freestream Mach numbers, similar to those cases with Roe's FDS scheme. Thus it is believed that the present adaptive dissipation model proposed to improve the stability and convergence characteristics of the point GS method also works well with other upwind schemes as well.

## 7. Conclusions

In the present study, an efficient and robust implicit operator for the upwind point Gauss–Seidel method has been developed for solving the compressible Euler equations. It was found that the amount of numerical dissipation in the implicit operator has a significant effect on the stability and convergence characteristics. For the robustness of the point Gauss–Seidel method, the numerical flux of the implicit operator needs to be more dissipative than that of the explicit operator. Also, the amount of numerical dissipation in the implicit operator should be determined carefully to achieve the efficiency and the robustness simultaneously. Based on these observations, a new scalar form of adaptive artificial dissipation model was developed for upwind implicit operators.

In order to validate the implicit operator with the new dissipation model, numerical experiments were conducted for flows ranging from subsonic to hypersonic speeds. For subsonic and transonic flow problems, both matrix and scalar forms of added dissipation worked well for improving the numerical stability, and the Jameson–Turkel operator and the present operator were unconditionally stable. Even though the two implicit operators had similar stability characteristics, the present operator always showed much better convergence rates than the Jameson–Turkel operator. For hypersonic flow problems, it was found that the matrix form of added dissipation was not robust enough for handling strong shock waves, and thus the Jameson–Turkel implicit operator suffered severe convergence degradation. Meanwhile the present implicit operator always showed good stability and convergence characteristics. It was concluded that the present implicit operator with a scalar form of adaptive artificial dissipation is more efficient and robust than other existing implicit operators for solving the compressible Euler equations over a wide range of flow problems.

## References

- [1] T.J. Barth, Analysis of implicit local linearization techniques for upwind and TVD algorithms, AIAA Paper87-0595, 1987.
- [2] A. Jameson, W. Schmidt, E. Turkel, Numerical solutions of the Euler equations by finite volume methods using Runge–Kutta time-stepping schemes, AIAA Paper 81-1259, 1981.

- 502 [3] T.H. Pulliam, J.L. Steger, Implicit finite-difference simulations of three-dimensional compressible flow, *AIAA J.* 18 (2) (1978) 159–  
503 167.
- 504 [4] A. Jameson, S. Yoon, Multigrid solution of the Euler equations using implicit schemes, *AIAA J.* 24 (11) (1986) 1737–1743.
- 505 [5] T.H. Pulliam, Artificial dissipation models for the Euler equations, *AIAA J.* 24 (12) (1986) 1931–1940.
- 506 [6] M.S. Liou, B. van Leer, Choice of implicit and explicit operators for the upwind differencing method, *AIAA Paper* 88-0624, 1988.
- 507 [7] J.R. Amaladas, H. Kamath, Implicit and multigrid procedures for steady-state computations with upwind algorithms, *Comput.*  
508 *Fluids* 28 (1999) 187–212.
- 509 [8] R.M. Beam, R.F. Warming, An implicit factored scheme for the compressible Navier–Stokes equations, *AIAA J.* 16 (4) (1978) 393–  
510 402.
- 511 [9] S.R. Chakravarthy, Relaxation methods for unfactored implicit upwind schemes, *AIAA Paper* 84-0165, 1984.
- 512 [10] Y. Saad, M.H. Schultz, GMRES: a generalized minimal residual algorithm for solving nonsymmetric linear systems, *J. Sci. Stat.*  
513 *Comput.* 7 (3) (1986) 856–869.
- 514 [11] W.K. Anderson, D.L. Bonhaus, An implicit upwind algorithm for computing turbulent flows on unstructured grids, *Comput. Fluids*  
515 23 (1) (1994) 1–21.
- 516 [12] N.T. Frink, Assessment of an unstructured-grid method for predicting 3-d turbulent viscous flows, *AIAA Paper* 96-0292, 1996.
- 517 [13] W.S. Oh, J.S. Kim, O.J. Kwon, Numerical simulation of two-dimensional blade–vortex interactions using unstructured adaptive  
518 meshes, *AIAA J.* 40 (3) (2002) 474–480.
- 519 [14] S. Yoon, A. Jameson, Lower-upper symmetric-Gauss–Seidel method for the Euler and Navier–Stokes equations, *AIAA J.* 26 (9)  
520 (1988) 1025–1026.
- 521 [15] M.J. Wright, G.V. Candler, M. Prampolini, Data-parallel lower–upper relaxation method for the Navier–Stokes equations, *AIAA J.*  
522 34 (7) (1996) 1371–1377.
- 523 [16] R.F. Chen, Z.J. Wang, Fast, block lower–upper symmetric Gauss–Seidel scheme for arbitrary grids, *AIAA J.* 38 (12) (2000) 2238–  
524 2245.
- 525 [17] D.L. Whitfield, L.K. Taylor, Discretized Newton-relaxation solution of high resolution flux-difference split schemes, *AIAA Paper* 91-  
526 1539, 1991.
- 527 [18] B. Koren, Defect correction and multigrid for an efficient and accurate computation of airfoil flows, *J. Comput. Phys.* 77 (1988) 183–  
528 206.
- 529 [19] W.K. Anderson, J.L. Thomas, B. van Leer, Comparison of finite volume flux vector splittings for the Euler equations, *AIAA J.* 24 (9)  
530 (1986) 1453–1460.
- 531 [20] V. Venkatakrishnan, Convergence to steady state solutions of the Euler equations on unstructured grids with limiters, *J. Comput.*  
532 *Phys.* 118 (1995) 120–130.
- 533 [21] P.E.O. Buelow, S. Venkateswaran, C.L. Merkle, Stability and convergence analysis of implicit upwind schemes, *Comput. Fluids* 30  
534 (2001) 961–988.
- 535 [22] R.W. MacCormack, T.H. Pulliam, Assessment of a new numerical procedure for fluid dynamics, *AIAA Paper* 98-2821, 1998.
- 536 [23] A.C. Taylor III, W.-F. Ng, R.W. Walters, Upwind relaxation methods for the Navier–Stokes equations using inner iterations, *J.*  
537 *Comput. Phys.* 99 (1992) 68–78.
- 538 [24] L. Mottura, L. Vigevano, M. Zaccanti, Factorized implicit upwind methods applied to inviscid flows at high Mach number, *AIAA*  
539 *Paper* 98-2822, 1998.
- 540 [25] A. Jameson, E. Turkel, Implicit schemes and LU decompositions, *Math. Comput.* 37 (156) (1981) 385–397.
- 541 [26] P.L. Roe, Approximate Riemann solvers, parameter vectors, and difference schemes, *J. Comput. Phys.* 43 (1981) 357–372.
- 542 [27] H. Luo, J.D. Baum, R. Löhner, A fast, matrix-free implicit method for compressible flows on unstructured grids, *J. Comput. Phys.*  
543 146 (1998) 664–690.
- 544 [28] D.L. Darmofal, K. Sui, A robust multigrid algorithm for the Euler equations with local preconditioning and semi-coarsening, *J.*  
545 *Comput. Phys.* 151 (1999) 728–756.
- 546 [29] W.Z. Strang, R.F. Tomaro, M.J. Grismer, The defining methods of *Cobalt*<sub>60</sub>: a parallel, implicit, unstructured Euler/Navier–Stokes  
547 flow solver, *AIAA Paper* 99-0786, 1999.
- 548 [30] D.J. Mavriplis, A. Jameson, Multigrid solution of the Navier–Stokes equations on triangular meshes, *AIAA J.* 28 (8) (1990) 1415–  
549 1425.
- 550 [31] D.L. De Zeeuw, A quadtree-based adaptively-refined Cartesian-grid algorithm for solution of the Euler equations, Ph.D. Thesis,  
551 University of Michigan, 1993.
- 552 [32] B. van Leer, Flux-vector splitting for the Euler equations, *Lect. Notes Phys.* 170 (1982) 507–512.
- 553 [33] W.K. Anderson, R.D. Rausch, D.L. Bonhaus, Implicit/multigrid algorithms for incompressible turbulent flows on unstructured grids,  
554 *J. Comput. Phys.* 128 (1996) 391–408.
- 555 [34] W.O. Valarezo, C.J. Dominik, R.J. McGhee, W.L. Goodman, K.B. Paschal, Multi-element airfoil optimization for maximum lift at  
556 high Reynolds numbers, *AIAA Paper* 91-3332, 1991.
- 557 [35] H.C. Yee, G.H. Klopfer, J.-L. Montagne, High-resolution shock-capturing schemes for inviscid and viscous hypersonic flows, *J.*  
558 *Comput. Phys.* 88 (1990) 31–61.
- 559 [36] A.N. Lyubimov, V.V. Rusanov, Gas flows past blunt bodies, *NASA TT-F* 715, 1973.
- 560 [37] F.S. Billing, Shock-wave shapes around spherical- and cylindrical-nosed bodies, *J. Spacecraft* 4 (6) (1967) 822–823.
- 561